

Light Curve Models of Convective Common Envelopes

N. Noughani^{a,c}, J. Nordhaus^{b,c}, M. Richmond^a, E.C. Wilson^d

^a*School of Physics and Astronomy, Rochester Institute of Technology, 1 Lomb Memorial Dr., Rochester, 14623, NY, USA*

^b*National Technical Institute for the Deaf, Rochester Institute of Technology, Rochester, 14623, NY, USA*

^c*Center for Computational Relativity and Gravitation, Rochester Institute of Technology, Rochester, 14623, NY, USA*

^d*Astronomy and Physics Department, Lycoming College, Williamsport, 17701, PA, USA*

Abstract

Common envelopes are thought to be the main method for producing tight binaries in the universe as the orbital period shrinks by several orders of magnitude during this phase. Despite their importance for various evolutionary channels, direct detections are rare, and thus observational constraints on common envelope physics are often inferred from post-CE populations. Population constraints suggest that the CE phase must be highly inefficient at using orbital energy to drive envelope ejection for low-mass systems and highly efficient for high-mass systems. Such a dichotomy has been explained by an interplay between convection, radiation and orbital decay. If convective transport to the surface occurs faster than the orbit decays, the CE self-regulates and radiatively cools. Once the orbit shrinks such that convective transport is slow compared to orbital decay, a burst occurs as the release of orbital energy can be far in excess of that required to unbind the envelope. With the anticipation of first light for the Rubin Observatory, we calculate light curve models for convective common envelopes and provide the time evolution of apparent magnitudes for the Rubin filters. Convection imparts a distinct signature in the light curves and lengthens the timescales during which they are observable. Given Rubin limiting magnitudes, convective CEs should be detectable out to distances of ~ 8 Mpc at a rate of ~ 0.3 day⁻¹ and provide an intriguing observational test of common envelope physics.

Keywords: Common Envelope Evolution, Stellar Convective Zones, Evolved Stars, Transient Sources

1. Introduction

The primary mechanism for producing close binaries that contain at least one compact object is thought to be common envelope (CE) evolution (Paczynski, 1976; Toonen and Nelemans, 2013; Kruckow et al., 2018; Canals et al., 2018). CEs often occur during post-main-sequence phases, when the radius of one component of the binary expands to hundreds of times its original size, significantly increasing the interaction cross section (Ivanova et al., 2012; Kochanek et al., 2014). In two-body systems, CEs may commence via direct engulfment, Roche Lobe overflow, or orbital decay via tidal dissipation (Nordhaus et al., 2010; Nordhaus and Spiegel, 2013; Chen et al., 2017), while dynamic effects can lead to plunge in for higher-order systems (Fabrycky and Tremaine, 2007; Thompson, 2011; Shappee and Thompson, 2013; Michaely and Perets, 2016). Two outcomes are possible: the companion survives and emerges in a post-CE binary (PCEB), or is destroyed, leaving a single star whose evolution has been significantly altered (Nordhaus et al., 2011).

The details of how energy is transferred from the orbit to the envelope is an active area of research and critical to predicting CE outcomes (Macleod et al., 2018; Chamandy et al., 2018b; Wilson and Nordhaus, 2019, 2020, 2022). If orbital energy is released inside convective regions, turbulent eddies distribute and carry this energy toward the surface where it could be lost from the system via radiation. If this occurs before the envelope is ejected, a larger supply of energy would be required before

the envelope could be unbound. Since low-mass and high-mass giant stars possess deep and vigorous convective zones, the interplay between orbital decay, convection, and radiation is necessary to understanding CE outcomes.

Despite this, current numerical simulations of CEs have not yet included convection or radiation due to computational complexity (Passy et al., 2011; Ricker and Taam, 2012; Iaconi and De Marco, 2019; Reichardt et al., 2020; Hatfull et al., 2021; González-Bolívar et al., 2022; Chamandy et al., 2023; Röpke and De Marco, 2023; Valsan et al., 2023). Analytic approaches, however, can incorporate convective and radiative effects in a physically-motivated manner, and have had success reproducing the observed populations of Galactic post-CE systems for M dwarf + white dwarf (WD) systems and short-period double white dwarfs (DWDs) (Wilson and Nordhaus, 2019, 2020). This contends with population synthesis studies that assign constant low efficiencies to the CE phase, but still overproduce long-period binaries (Politano and Weiler, 2007; Davis et al., 2009; Zorotovic et al., 2010; Toonen et al., 2017).

Recently, observations of high-mass, post-CE binaries in the Magellanic clouds imply that the CE phase must be highly *efficient* in using orbital energy to drive envelope ejection, while Galactic observations of low-mass, post-CE binaries imply that the CE phase must be highly *inefficient* (Wilson and Nordhaus, 2022). Such a dichotomy occurs because, in high-mass systems, the time required for convection to transport orbital energy to the surface is often long compared to orbital decay, and

thus the orbital energy can only contribute to envelope ejection. For low-mass CE phases, the opposite is often the case: convective transport to the surface occurs rapidly, allowing the CE to self-regulate and cool via radiative losses.

Despite the importance of the common envelope phase for determining binary evolution outcomes, direct observational tests of CEs are elusive as the evolutionary timescales are short (e.g. months to years), and the predicted transient signatures are faint (Blagorodnova et al., 2016). With first light for the Vera C. Rubin Observatory approaching, there has been renewed interest in CE transient signatures, particularly because of their short timescales.

Motivated by the success that incorporating convection and radiation has had in reproducing Galactic post-CE populations (Wilson and Nordhaus, 2019, 2020, 2022), we investigate how those effects impact light-curve predictions. Most noticeably, if the CE *is* convective, orbital energy can be transported to the surface and lost from the system. If this occurs faster than the orbit decays, the CE radiatively cools, and the luminosity of the system is then expected to increase *gradually* while the radius of the primary remains roughly steady. However, if the CE is *not* convective, the orbital energy must be used to raise the negative binding energy of the envelope. In this case, a sudden rise in luminosity upon engulfment is expected as the envelope immediately expands (Hatfull et al., 2021; Matsumoto and Metzger, 2022).

In this work, we hypothesize that convective eddies are able to carry energy produced by the orbiting secondary mass out of the primary star’s envelope, increasing the overall brightness without contributing to unbinding the primary star’s envelope. Once the orbit shrinks such that convective transport is slow compared to orbital decay, a burst occurs as the release of orbital energy can be far in excess of that required to unbind the envelope. Since this energy can only act to drive ejection, the CE expands and more closely resembles previous predictions for CE light curves. The lengthening of the observable timescales for convective CEs compared to non-convective CEs makes for an intriguing observational test in the era of time domain surveys.

The structure of this paper is as follows: in Section 2, we provide an overview of the CE interaction, the stellar models employed, and our assumptions. In Section 3, we detail how the combined effects of convection and radiation qualitatively impact CE outcomes. In Section 4, we demonstrate how convection changes light-curve predictions for low-mass CE systems and give approximate observational values that can be used for real data comparison, and specific values for the Vera C. Rubin Observatory. In Section 5, we discuss implications and estimate detection rates given Rubin limiting magnitudes. Finally, we conclude and discuss future work in Section 6.

2. Common Envelope Evolution

The outcome of a CE phase is dependent on the physics of the interaction, the structure of the envelope, and the details of energy and angular momentum transport during the CE phase

(Icko and Livio, 1993). A commonly-used condition for estimating whether the envelope is ejected is given by:

$$E_{\text{bind}} \leq \bar{\alpha}_{\text{eff}} \Delta E_{\text{orb}}, \quad (1)$$

where E_{bind} is the energy required to unbind the envelope, ΔE_{orb} is the orbital energy released during inspiral, and $\bar{\alpha}_{\text{eff}}$ is a constant, and sometimes averaged, efficiency value with which liberated orbital energy can be used to unbind the CE (Tutukov and Yungelson, 1979; Iben and Tutukov, 1984; Webbink, 1984; Livio and Soker, 1988; De Marco et al., 2011; Wilson and Nordhaus, 2019, 2022). How efficiently orbital energy can be tapped to drive envelope ejection, and whether this condition is sufficient, is a subject of active research (Ivanova et al., 2015; Nandez et al., 2015; Chamandy et al., 2018a; Grichener et al., 2018; Ivanova, 2018; Soker et al., 2018; Wilson and Nordhaus, 2019, 2020, 2022).

Numerical simulations of CEs have had difficulty unbinding and producing post-CE orbits consistent with observations even though there is often sufficient energy available in the orbit (Ricker and Taam, 2008, 2012; Passy et al., 2011; Ohlmann et al., 2015; Chamandy et al., 2018a). This led to suggestions and debate about whether the inclusion of additional energy sources such as those from accretion, jets or recombination, as well as from processes on longer timescales could aid ejection (Ivanova et al., 2015; Nandez et al., 2015; Soker, 2015; Kurwita et al., 2016; Sabach et al., 2017; Glanz and Perets, 2018; Grichener et al., 2018; Ivanova, 2018; Kashi and Soker, 2018; Soker et al., 2018; Reichardt et al., 2020; Schreier et al., 2021; Lau et al., 2022; Valsan et al., 2023).

Independent of energy source(s), simulations of CEs neglect important processes in post-main-sequence stars, namely the presence of vigorous and deep convective zones and the effects of radiation. In conjunction, convection and radiation allow the CE to self-regulate and cool until orbital decay occurs faster than convective transport. This allows the orbit to shrink substantially and ejection to occur much deeper in the envelope. The success this approach has had in reproducing population observations of post-CE M dwarf + white dwarf binaries, double white dwarfs and massive star binaries, motivates this work (Wilson and Nordhaus, 2019, 2020, 2022).

2.1. Stellar Models

This work uses the open-source stellar evolution code MESA to generate spherically-symmetric models of stellar interiors (release 10108; Paxton et al. 2011, 2018). Models were produced for zero-age-main-sequence (ZAMS) masses ranging from $M_{\star} = 1 M_{\odot}$ to $6 M_{\odot}$, where M_{\star} denotes the mass of the primary star in the system, in $1 M_{\odot}$ increments from the pre-main-sequence to the white dwarf phase. The choice of initial metallicity was solar ($z = 0.02$). A Reimer’s mass-loss prescription with $\eta_R = 0.7$ was used for the RGB phase, while a Bloeker mass-loss prescription with $\eta_B = 0.15$ was used for the 1 and $2 M_{\odot}$ primaries, and $\eta_B = 0.7$ for the 3– $6 M_{\odot}$ primaries on the AGB (Reimers, 1975; Bloeker, 1995). These choices ensured the models matched the observed initial-final mass relationship (IFMR) derived from cluster observations (Cummings et al., 2018; Hollands et al., 2023).

For each evolutionary model, we chose the point in time when the star had evolved to its maximum radius. This yields the largest cross section for CE interactions, and makes it a reasonable time for a CE event to occur, as the primary occupies its greatest possible volume. Additionally, at this point in the evolution, the deep convective regions in the star result in strong tidal torques that act to decrease the orbits of companions that were not previously engulfed during the primary’s radial expansion. Companions that avoid engulfment, but initially orbited within ~ 10 AU, could plunge into the envelope as tidal dissipation deposits orbital energy in the primary (Villaver and Livio, 2009; Nordhaus et al., 2010; Nordhaus and Spiegel, 2013).

For each primary, we selected five companions for a total of thirty possible CE interactions. We define the mass ratio of the system as $q \equiv m_2/M_\star$, where $m_2 < M_\star$. For primaries with ZAMS masses between 1 and 4 M_\odot , we chose mass ratios of $q = 0.02, 0.05, 0.08, 0.1$, and 0.2 , which correspond to companion masses between 0.02 M_\odot ($\sim 21 M_{\text{Jupiter}}$) and 0.8 M_\odot . For primaries with ZAMS masses of 5 and 6 M_\odot , mass ratios of $q = 0.02, 0.05, 0.08, 0.1$, and 0.15 were selected, corresponding to companion masses between 0.1 M_\odot and 0.9 M_\odot . These secondaries were chosen such that convection in the primary’s envelope could accommodate the luminosity produced during inspiral while remaining subsonic in nature. In addition, each system possessed sufficient orbital energy to eject the envelope and emerge in a post-CE binary before tidal disruption occurs (Guidarelli et al., 2019, 2022). Note that our models do not calculate any precursor emission, such as the emission that stripping the weakly bound outer layer of the star would produce (Matsumoto and Metzger, 2022).

3. Convective Common Envelopes

The time required for the orbit of the secondary mass in a CE to fully decay, typically referred to as the inspiral timescale, is given as,

$$t_{\text{inspiral}} = \int_{r_i}^{r_{\text{shred}}} \frac{\left(\frac{dM}{dr} - \frac{M}{r}\right) \sqrt{v_r^2 + (\bar{v}_\phi^2 + c_s^2)^2}}{4\xi\pi G m_2 r \rho} dr, \quad (2)$$

where c_s is the speed of sound, G is the gravitational constant, ρ is the gas density, M is the mass interior to the orbit, \bar{v}_ϕ is the orbital velocity, r is the radial position, r_i is the initial radial position, and r_{shred} is the tidal shredding radius (Nordhaus and Blackman, 2006). As the orbit shrinks, if the envelope is not ejected, tidal disruption of the companion will occur and result in the formation of an accretion disk inside the CE (Guidarelli et al., 2022). This occurs where the differential gravitational force across the companion exceeds its own self gravity. Therefore, we take the tidal shredding radius as $r_{\text{shred}} \approx R_2(2M_{\text{core}}/m_2)^{1/3}$, where M_{core} is the mass of the core of the primary star, m_2 is the mass of the companion, and R_2 is the radius of the companion.

We consider three types of companions: planets, brown dwarfs and main-sequence stars and determine their radii, R_2 , based on the type and the mass. For $m_2 > 0.077M_\odot$, we assume the companion is a main-sequence star with radius given by

$$R_2 = \left(\frac{m_2}{M_\odot}\right)^{0.92} R_\odot, \quad (3)$$

(Reyes-Ruiz and López, 1999). For $0.0026M_\odot < m_2 < 0.077M_\odot$, the companion is assumed to be a brown dwarf (Burrows et al., 1993) with radius given by:

$$R_2 = R_\odot \left[0.117 - 0.054 \log^2 \left(\frac{m_2}{0.0026M_\odot} \right) + 0.024 \log^3 \left(\frac{m_2}{0.0026M_\odot} \right) \right]. \quad (4)$$

Finally, the planetary companions we consider are gas giants and assigned a radius equal to that of Jupiter (Zapolsky and Salpeter, 1969).

The orbital velocity \bar{v}_ϕ is assumed to be $\bar{v}_\phi = v_\phi - v_{\text{env}} \approx v_\phi$, as the envelope of the primary rotates slowly compared to the orbit for RGB/AGB stars (Nordhaus et al., 2007). Additionally, ξ , is a dimensionless constant that accounts for the Mach number of the companion as it moves through the envelope (Park and Bogdanović, 2017). Because the motion of the companion is mildly supersonic, we take $\xi = 4$ and note that the ejection efficiency $\bar{\alpha}_{\text{eff}}$ is not sensitive to this parameter for the mass ratios considered here (Shima et al., 1985).

3.1. Effects of Convection

Red Giant and Asymptotic Giant Branch stars possess convective zones that extend from the surface deep into the interior, often making them almost fully convective. During inspiral, energy is transferred from the orbit to the envelope. If this energy is liberated in a convective region, it will be redistributed in the CE and transported outward. The convective transport timescale is defined as

$$t_{\text{conv}} = \int_r^{R_\star} \frac{1}{v_{\text{conv}}[r']} dr', \quad (5)$$

and represents the time required for a convective eddy to migrate from a position in the interior to the surface. Here, we take v_{conv} as the unperturbed convective velocities associated with the primary’s envelope.¹

Figure 1 compares the convective transport timescales (Eqn. 5) for the 1 M_\odot (thin-black curve) and the 6 M_\odot (thick-black curve) primaries to the orbital decay timescales (Eqn. 2) for ten CE configurations. Five companions, represented by various colors and line types, are shown for each primary. The companions associated with the 1 M_\odot primary represent mass ratios of 0.02, 0.05, 0.08, 0.1, and 0.2, while the companions associated with the 6 M_\odot primary represent mass ratios of 0.02, 0.05, 0.08, 0.1, and 0.15. Each curve terminates in “x” markers for the 1 M_\odot primary and “▲” markers for the 6 M_\odot

¹The convective transport timescales calculated in this work are upper limits as any acceleration of the convective eddies would result in a shorter time required to reach the surface.

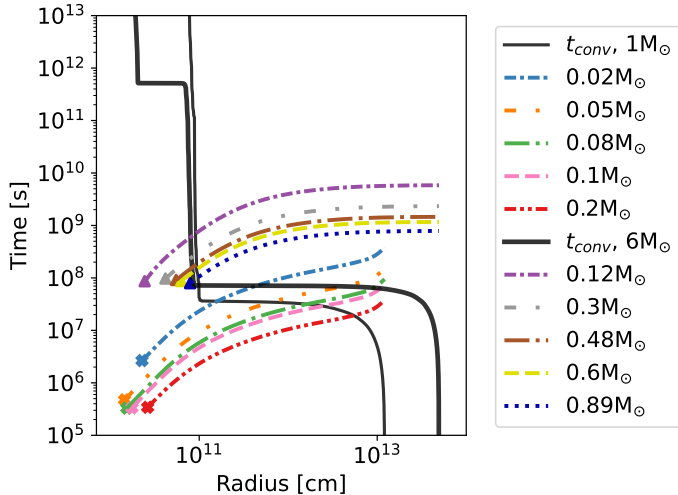


Figure 1: Above are the inspiral and convective timescales for primary stars of 1 and 6 M_{\odot} . The convective timescales define the time, on the y-axis, required for convection in the primary to carry energy from point r , on the x-axis, out to the surface (R_{\star}). These are shown as black lines for the 1 (thin) and 6 (thick) M_{\odot} primaries. The inspiral timescales define the time required for the companion to inspiral from its current radius to the center of the primary star. The five companions of the 1 M_{\odot} primary (0.02, 0.05, 0.08, 0.1, and 0.2 M_{\odot}) and the five companion masses of the 6 M_{\odot} primary (0.12, 0.3, 0.48, 0.6 and 0.89 M_{\odot}) are shown above using differing lines styles and colors. The location where each companion shreds is marked with an "x" (1 M_{\odot} primary) or a "▲" (6 M_{\odot} primary).

primary where tidal disruption occurs. So long as the inspiral timescales (colorful curves) are greater than the convective timescales (black curves), convection can successfully carry energy out to the surface of the primary star.

As the orbit decays, the energy released is given by

$$\Delta E_{\text{orb}} = \frac{Gm_2}{2} \left(\frac{M[r_i]}{r_i} - \frac{M[r]}{r} \right). \quad (6)$$

If this energy is liberated in the convective regions defined via timescale comparisons (see Figure 1), it can be redistributed in the CE and transported outward, eventually leaving the primary in the form of light. The maximum luminosity that convection can accommodate while retaining its subsonic nature is given by

$$L_{\text{conv,max}} = \beta 4\pi\rho r^2 c_s^3, \quad (7)$$

where we assume $\beta = 5$ (Grichener et al., 2018). As the orbit decays, the drag luminosity produced is given by

$$L_{\text{drag}} = \xi\pi r_{\text{acc}}^2 \rho v_{\phi}^3, \quad (8)$$

where $r_{\text{acc}} = 2Gm_2/(v_{\phi}^2 + c_s)$ is the accretion radius measured from the center of the primary (Nordhaus and Blackman, 2006). Where the drag luminosity exceeds the maximum convective luminosity, convection may transition to the supersonic regime. In such a case, any shocks that develop would contribute to raising the negative binding energy of the envelope.

Figure 2 displays the maximum amount of luminosity convection can carry for the 1 M_{\odot} (thin-black curve) and 6 M_{\odot} (thick-black curve) primaries. As the orbit decreases, the drag

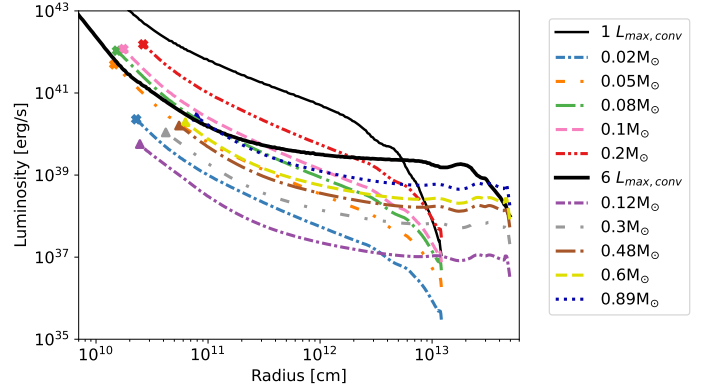


Figure 2: The maximum amount of luminosity convection can carry out of the primary stars are shown via thin (1 M_{\odot}) and thick (6 M_{\odot}) solid black lines labeled $L_{\text{max,conv}}$. The drag luminosities produced during each CE are shown with the varying dashed and coloured lines consistent with Figure 1. The radial limits where the companions are destroyed via tidal disruption are marked by an "x" (1 M_{\odot} primary) or a "▲" (6 M_{\odot} primary).

luminosity generated for each binary configuration is presented in various color and line types (consistent with Figure 1) with the mass of the corresponding companions listed in the legend. The "x" markers for the 1 M_{\odot} primary and "▲" markers for the 6 M_{\odot} primary indicate where each companion is tidally disrupted. Note that convection can accommodate the totality of the luminosity generated during inspiral for the binaries presented in this work.

The minimum energy required to unbind the primary's envelope is given as

$$E_{\text{bind}} = - \int_M^{M_{\star}} \frac{GM[r]}{r} dm[r], \quad (9)$$

where M_{\star} is the mass of the primary star. By calculating the binding energy directly from stellar evolution models, we avoid the need for λ -formalisms that approximate a star's gravitational binding energy when the interior structure is not known (De Marco et al., 2011).

The binding energy as a function of position for the 1 M_{\odot} and 6 M_{\odot} primaries are shown in solid thin and thick black curves respectively in Figure 3. For each primary, the energy released as the orbits decay are shown in the same color and line types as Figures 1 and 2. Note where $t_{\text{conv}} < t_{\text{inspiral}}$, we assume the orbital energy is transported to the surface and radiated away, and therefore does not contribute to unbinding the envelope. As the CE phase continues, orbital decay will eventually occur faster than convection can transport the energy to the surface. This can happen while the companion still orbits in a convective zone, or will occur when it reaches a radiative zone. In either case, the liberated orbital energy cannot escape the system and must be used to raise the negative binding energy of the envelope. Therefore, we assume orbital energy can only contribute to unbinding the envelope when $t_{\text{inspiral}} < t_{\text{conv}}$. Given these constraints, there is sufficient energy in the orbits to eject the envelope and emerge as a post-CE binary for all systems in this work (see Figure 3).

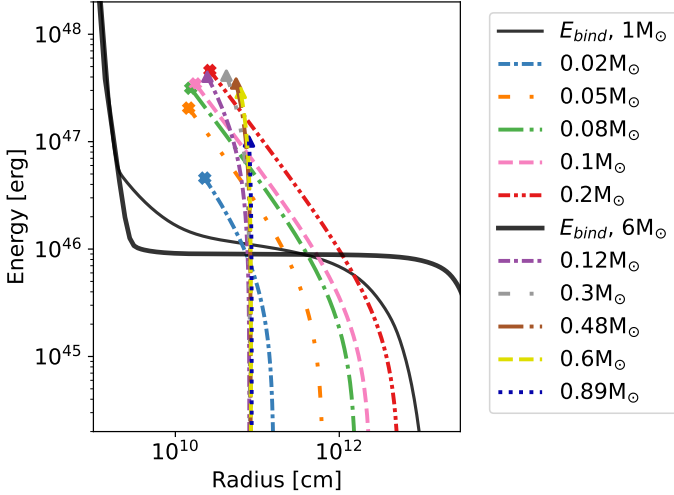


Figure 3: Illustrated above are the inspiral and binding energies for two primary masses (1 and $6 M_{\odot}$), with position along the radius of the primary on the x-axis in centimeters and energy in ergs on the y-axis. The binding energies for both are shown in thin ($1 M_{\odot}$) and thick ($6 M_{\odot}$) solid black lines, and represent the minimum energy required to unbind that portion of the primary’s envelope at every point along its radius as a function of position. The companion’s inspiral energies, shown in the varying colors and line patterns of Figures 1 and 2, all intersect with the binding energy limits before reaching their shredding radii, illustrated via an “x” ($1 M_{\odot}$) or a “▲” ($6 M_{\odot}$). Therefore, all the companions shown unbind the primary’s envelope and are expected to form close binary pairs.

4. Light Curve Modeling

Our CE evolution consists of two distinct phases: (i.) a self-regulated phase and (ii.) an ejection phase. During the self-regulated phase, orbital energy is rapidly transported to the surface and radiated away. Since we explicitly assume this energy escapes and does not contribute to unbinding the envelope, the stellar radius remains constant while the luminosity of the system increases. The ejection phase occurs once $t_{\text{inspiral}} < t_{\text{conv}}$, as the liberated orbital energy cannot be lost and must be used to drive ejection. When this occurs, it can be the case that energy much in excess of the binding energy is supplied rapidly (see Figure 3).

The light curve for a convective CE therefore also consists of two parts. During the self-regulated phase, the drag luminosity drives the increase in the total luminosity of the system. Once ejection occurs, the evolution of the luminosity is dominated by radial expansion and similar to that of Type IIP supernovae, which are characterized by a plateau phase (Chugai, 1991; Popov, 1993; Kasen and Woosley, 2009). Note that the application of Type IIP supernova light curve modeling to low-mass, non-convective CE and merger events has been previously studied in detail (Ivanova et al., 2013; Hatfull et al., 2021; Matsumoto and Metzger, 2022; Chen and Ivanova, 2024).

4.1. Luminosity Evolution During Ejection

For the ejection phase, we employ a simple model where we assume that the gas is optically thick at temperatures above a chosen ionization temperature, T_{ion} , and optically thin at lower temperatures (Popov, 1993). This results in a two-zone model

in the envelope with a recombination front that starts at time t_i and initial position $r = R_i$ serving as the boundary. We define an envelope expansion timescale, $t_{\text{exp}} \equiv R_{\star}/v_{\text{exp}} = R_{\star} (3M/10E)^{1/2}$, where R_{\star} is the radius of the primary star, v_{exp} is the expansion velocity, M is the mass of the ejected envelope, and E is the energy of the ejected envelope, which we take to be equal to the orbital energy that is released at the location where the envelope is ejected (Figure 3). In combination with the photon diffusion timescale, $t_d = 9\kappa M/4\pi^3 c R_{\star}$, we define a characteristic timescale on which changes occur as $t_a \equiv (2t_d t_{\text{exp}})^{1/2}$. We choose an ionization temperature of 5000 K (Popov, 1993) for all models, and set the opacity to the corresponding value at that temperature in the primary’s interior. This results in typical expansion speeds ranging from ~ 50 to 100 km/s, consistent with outflow ejecta in proto-planetary and planetary nebulae (Bujarrabal et al., 2001; Lorenzo et al., 2021).

Recombination begins at moment t_i , which is determined by equating the luminosity on the interior-side and exterior-side of the recombination front such that

$$\frac{E}{2t_d} e^{-t_i^2/t_a^2} = 8\pi\sigma_{\text{SB}}v_{\text{exp}}^2 t_i^2 T_{\text{ion}}^4, \quad (10)$$

where σ_{SB} is the Stefan-Boltzmann constant (Popov, 1993). Note that t_i is measured from the moment expansion begins, i.e. the moment orbital decay occurs faster than convective transport. The time evolution of the luminosity during the plateau phase is then given by

$$L_{\text{bol}} = 8\pi\sigma_{\text{SB}}T_{\text{ion}}^4 v_{\text{exp}}^2 \left[t_i t \left(1 + \frac{t_i^2}{3t_a^2} \right) - \frac{t^4}{3t_a^2} \right]. \quad (11)$$

During the ejection phase, the envelope expands and cools, and formation of dust may initially obscure the natal white dwarf (Bermúdez-Bustamante et al., 2024). Observations of post-RGB/AGB systems often show a breaking of symmetry with dusty tori in the orbital plane accompanied by bipolar outflows or jets perpendicular to the orbital plane (van Winckel, 2003). Such nebular shaping is an expected outcome of CE evolution and consistent with systems in which the linear momentum and energy in the outflows far surpass what single stars can achieve (Bujarrabal et al., 2001; Nordhaus et al., 2007). Thus, the evolution of the post-plateau luminosity depends on orientation and whether the hot, natal white dwarf can be observed, perhaps through cavities in the ejecta caused by jets clearing material. We calculate upper limits for the luminosity assuming that the white dwarf core is visible after the envelope expands for one year. Given our range of expansion velocities, this typically occurs when the envelope reaches ten to twenty astronomical units.

Figure 4 shows the full time evolution of the light curves for all thirty binary configurations, with panels representing primary mass increasing top to bottom and then left to right. The colors of the curves and their line styles are consistent with the previous figures in this paper, but are shown in terms of the corresponding mass ratios. The $1 M_{\odot}$ primary star plot also includes grey boxes, which denote all the points (but one, the final

WD luminosity) where an apparent magnitude was calculated for the models, as described in the following section.

We note that for all models, the evolution of the light curve is dominated by the self-regulated stage rather than the ejection phase. Convection extends the time required until envelope ejection occurs as energy is lost from the system. The imprint of the drag luminosity becomes the defining characteristic of the light curves for these events, and provides a means of identification of a CE in progress, pre-envelope ejection.

4.2. Expected Observational Magnitudes

The Vera C. Rubin Observatory’s Simonyi Survey telescope (Željko Ivezić et al., 2019) will measure targets in AB magnitude; therefore, we make our anticipated magnitude calculations in this system. Apparent magnitudes were derived for each model by applying a blackbody approximation over a broad wavelength range. We calculated a flux by integrating over the filter transmission curves. These curves were normalized for integration for each of the telescope’s filters across their respective wavelength ranges (Kahn et al., 2010). We calculated several properties for each filter: a central wavelength, λ_c , equivalent width in wavelength, Δ_λ , and equivalent width in frequency, Δ_ν . We integrated the flux density of each model over each respective equivalent wavelength range to derive an overall flux, Q , in each of the telescope’s passbands.

We then divided this flux by the filter width Δ_ν , to convert this flux into a flux density per unit frequency, $\Phi_\nu = Q/\Delta_\nu$. We use Φ_ν to calculate the AB magnitude:

$$m = -2.5 \log \left(\frac{\Phi_\nu}{\Phi_0} \right), \quad (12)$$

where Φ_0 is the zero point flux density for the AB magnitude system. We calculated these magnitudes at varying distances by scaling our flux density as $f\Phi_\nu$, where $f = R_p^2/D^2$, R_p is the radial size of the photosphere, and D is the distance to the system.

In Figure 5, we present apparent magnitudes corresponding to seven discrete times during CE evolution. For each binary, we choose six of these times by uniformly sampling the corresponding light curve between its maximum value and 1.1 times its minimum value (see gray boxes in top-left panel of Figure 4). The seventh point is taken after the envelope is ejected and represents the earliest time the natal white dwarf may be visible. All panels in Figure 5 depict three of the six Rubin Observatory bands – u-band (purple symbols), r-band (green symbols) and y-band (red symbols) – at two distances, 100 kiloparsecs (triangles) and 8000 kiloparsecs (circles). The limiting magnitudes for the telescope are also shown on each plot in horizontal lines with colors corresponding to their respective filters (Kahn et al., 2010). Apparent magnitudes that are dimmer than the corresponding filter’s limiting magnitude will not be detectable by the instrument in that band.

Apparent magnitudes of 30 common envelope systems were calculated and compared to the Rubin filter limiting magnitudes, and a representative sample are shown in Figure 5, again shown at the seven discrete times from Figure 4. Tables 1-6

Time [yrs]	u	g	r	i	z	y
4.36	3.50	0.219	-1.48	-2.34	-2.69	-1.11
8.32	0.172	-2.33	-3.43	-3.96	-4.10	-2.35
10.63	-2.35	-4.27	-4.91	-5.20	-5.19	-3.31
11.23	-4.26	-5.75	-6.06	-6.17	-6.05	-4.08
11.49	-5.72	-6.89	-6.96	-6.95	-6.75	-4.72
11.66	-6.71	-8.17	-8.46	-8.56	-8.44	-6.46
12.68	1.11*	-0.708*	1.24*	1.55*	1.93*	4.13*

Table 1: The table below shows the absolute magnitude for the 1 M_\odot primary and 0.02 M_\odot companion. The times chosen are those marked by the squares in Figure 4 and are measured from the start of the CE phase. The symbol * denotes when we’ve calculated upper limits to the emission.

Time [yrs]	u	g	r	i	z	y
10.36	3.11	-0.547	-2.54	-3.57	-4.02	-2.53
13.35	0.228	-2.76	-4.23	-4.97	-5.23	-3.59
13.75	-2.11	-4.56	-5.60	-6.11	-6.23	-4.46
13.94	-4.02	-6.02	-6.72	-7.05	-7.05	-5.19
14.03	-5.56	-7.21	-7.64	-7.82	-7.74	-5.80
14.21	-6.10	-7.97	-8.56	-8.83	-8.80	-6.90
15.26	-1.16*	-1.56*	-1.03*	-0.717*	-0.332*	1.87*

Table 2: The table below shows the absolute magnitude for the 2 M_\odot primary and 0.04 M_\odot companion. The symbol * denotes when we’ve calculated upper limits to the emission.

list absolute magnitudes in all six instrument bands (u, g, r, i, z, y) for the lowest mass-ratio system for each primary star, also at the seven discrete times described in Figure 4. Note that these systems produce the faintest predicted signatures while still being detectable, thereby implying that higher-mass ratio systems at the same distance will also be observable. The last line of each table provides a magnitude consistent with the upper luminosity limit if the hot, natal white dwarf is visible to the observer.

5. Results and Analysis

The Rubin Observatory will observe the southern sky every few nights for a decade (Željko Ivezić et al., 2019). Given the limiting magnitudes for the Rubin Observatory instrument, we calculate the total time during which a common envelope event is visible and present the results in Figure 6. The ordinate shows the distance to the CE event from the Earth while the abscissa presents the total time the CE can be observed, measured in years. Color and line styles are consistent with previous fig-

Time [yrs]	u	g	r	i	z	y
4.59	2.53	-0.99	-2.88	-3.85	-4.26	-2.75
6.56	-0.406	-3.24	-4.60	-5.28	-5.50	-3.83
7.06	-2.76	-5.05	-5.98	-6.43	-6.51	-4.71
7.23	-4.65	-6.51	-7.10	-7.36	-7.33	-5.44
7.33	-6.16	-7.68	-8.00	-8.13	-8.02	-6.05
7.53	-6.78	-8.53	-9.03	-9.25	-9.19	-7.27
8.59	-1.20*	-1.60*	-1.07*	-0.756*	-0.372*	1.83*

Table 3: The table below shows the absolute magnitude for the 3 M_\odot primary and 0.06 M_\odot companion. The symbol * denotes when we’ve calculated upper limits to the emission.

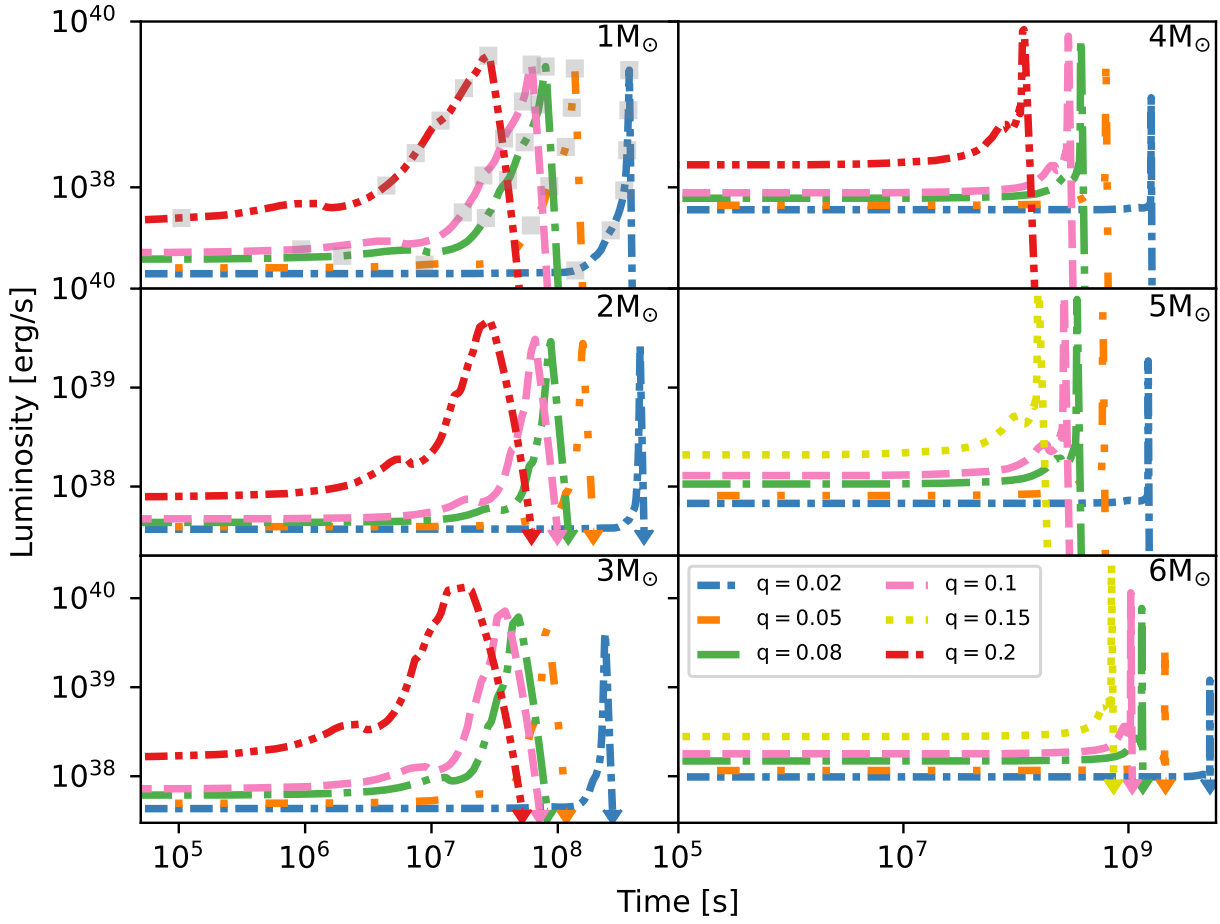


Figure 4: Time evolution of the predicted light curves for convective common envelopes are shown from top to bottom, then left to right, for primary masses of 1, 2, 3, 4, 5, and 6 M_{\odot} . For each primary, five CE light curves for different mass ratios are displayed with various colors and line styles. The 1 M_{\odot} primary plot includes grey boxes representing times where apparent magnitudes were calculated (see Section 4.2 for more detail). For each CE, we choose six of these times by uniformly sampling the corresponding light curve between its maximum value and 1.1 times its minimum value in log-space. The seventh point is taken after the envelope is ejected and represents an upper limit on the magnitude if the natal white dwarf were visible one year post-CE expulsion (depicted by upper limit triangle symbols above).

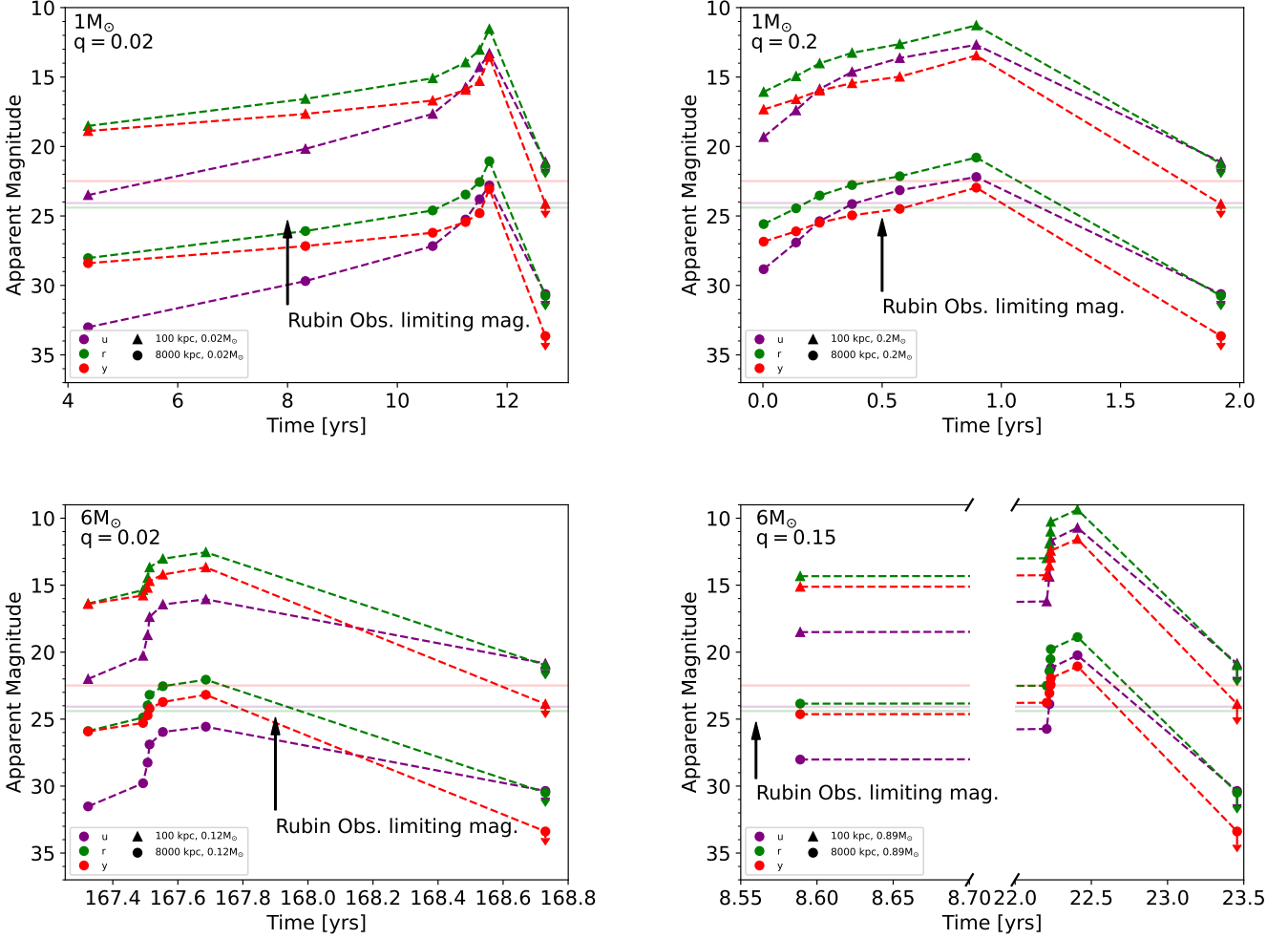


Figure 5: Apparent AB magnitudes for the $1 M_{\odot}$ primary with the smallest mass ratio system ($q = 0.02$; top left) and the largest mass ratio system ($q = 0.2$; top right) and the $6 M_{\odot}$ primary with the smallest mass ratio system ($q = 0.02$; bottom left) and the largest mass ratio system ($q = 0.15$; bottom right). Each plot shows three of the six Rubin filters, namely, u, r, and y. The semi-transparent, horizontal lines on each plot display the limiting magnitudes for the instrument, where the colors are consistent with each filter. Magnitudes are shown for two distances: 100 kpc (triangles) and 8000 kpc (circles). The points illustrated are those sampled from various epochs in the light curves as described in Section 4.2 and shown in Fig. 4. The last evolutionary point represents an upper limit assuming the natal white dwarf is visible.

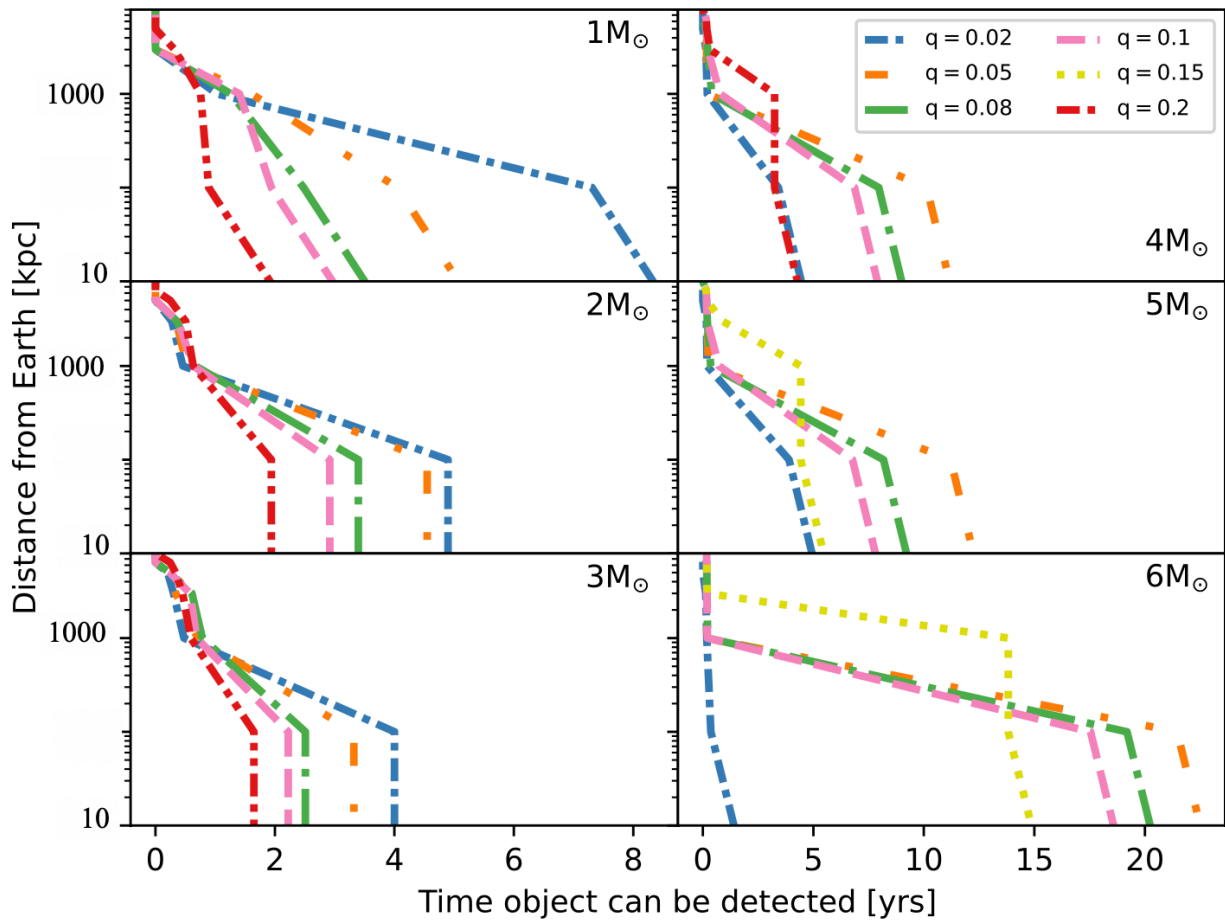


Figure 6: Above from top to bottom, then left to right, are plots demonstrating how long these convective CE systems are expected to be observed by the Rubin Observatory instrument, with time along the x-axis, for distances up to 8000 kpc, shown along the y-axis, for primary masses of 1, 2, 3, 4, 5, and 6 M_{\odot} with their respective five companion masses in various colors and line styles. The companions represent mass ratios of 0.02, 0.05, 0.08, 0.1 and 0.2 (primaries 1-4 M_{\odot}), and 0.02, 0.05, 0.08, 0.1, and 0.15 (primaries 5 and 6 M_{\odot}). As the LSST dataset is anticipated to span 10 years, many of the CE systems shown are ideal candidates and have a high likelihood of being observed by the telescope.

Time [yrs]	u	g	r	i	z	y
47.08	2.90	-0.820	-2.86	-3.92	-4.38	-2.91
50.19	0.715	-2.49	-4.14	-4.98	-5.30	-3.71
50.29	-1.16	-3.93	-5.24	-5.89	-6.10	-4.40
50.33	-2.78	-5.18	-6.19	-6.68	-6.79	-5.01
50.35	-4.17	-6.25	-7.01	-7.36	-7.39	-5.54
50.49	-4.50	-6.72	-7.60	-8.02	-8.08	-6.26
51.52	1.39*	0.995*	1.52*	1.84*	2.22*	4.42*

Table 4: The table below shows the absolute magnitude for the 4 M_{\odot} primary and 0.08 M_{\odot} companion. The symbol * denotes when we've calculated upper limits to the emission.

Time [yrs]	u	g	r	i	z	y
43.65	2.32	-1.29	-3.25	-4.26	-4.69	-3.20
47.28	0.071	-3.02	-4.57	-5.35	-5.64	-4.03
47.35	-1.85	-4.49	-5.69	-6.29	-6.46	-4.74
47.38	-3.48	-5.74	-6.65	-7.08	-7.16	-5.35
47.39	-4.87	-6.82	-7.47	-7.77	-7.76	-5.89
47.54	-5.31	-7.38	-8.14	-8.49	-8.51	-6.66
48.58	1.15*	0.748*	1.28*	1.59*	1.97*	4.17*

Table 5: The table below shows the absolute magnitude for the 5 M_{\odot} primary and 0.1 M_{\odot} companion. The symbol * denotes when we've calculated upper limits to the emission.

Time [yrs]	u	g	r	i	z	y
167.11	2.00	-1.64	-3.62	-4.64	-5.08	-3.60
167.28	0.272	-2.97	-4.64	-5.48	-5.81	-4.23
167.29	-1.27	-4.15	-5.54	-6.23	-6.46	-4.80
167.30	-2.62	-5.19	-6.33	-6.89	-7.04	-5.30
167.34	-3.56	-5.96	-6.97	-7.46	-7.57	-5.79
167.47	-3.95	-6.40	-7.46	-7.97	-8.10	-6.33
168.52	0.847*	0.448*	0.976*	1.29*	1.67*	3.87*

Table 6: The table below shows the absolute magnitude for the 6 M_{\odot} primary and 0.12 M_{\odot} companion. The symbol * denotes when we've calculated upper limits to the emission.

ures. Note that we define visibility such that the CE event is detectable in all filters at all discrete time points in its evolution. Thus, visibility is a measure of the total time during which the Rubin Observatory could observe a common envelope event.

Figure 6 shows that for a large combination of primary masses and mass ratios, common envelopes can be detected by Rubin for galactic and extra-galactic sources. As the primary mass increases, the differences between convective CEs and non-convective CEs become more prominent. For example, for a 1 M_{\odot} primary, the observable timescale increases by 22 days for the highest mass ratio system ($q = 0.2$) and by 146 days for the lowest mass ratio system ($q = 0.02$) compared to the non-convective case. For a 6 M_{\odot} primary, the observable timescale lengthens by 21 years for a system with $q = 0.15$ and 124 years for a system with $q = 0.02$. Given the duration of Rubin operations, distinguishing between convective and non-convective CEs should be possible.

To estimate the number of CE events that Rubin might observe, we first calculate an approximate number of CE events occurring at any point in time in the Milky Way as:

$$N_{\text{MW}} \sim f_{\text{CE}} n_{\text{s,MW}} t_{\text{CE}} / \bar{t}, \quad (13)$$

where N_{MW} is the number of CEs occurring in the Milky Way, \bar{t} is the average lifetime of a typical star, t_{CE} is the timescale for a typical CE phase, $n_{\text{s,MW}}$ is the number of stars in the Milky Way, and f_{CE} is the fraction of these stars which could incur a CE. Taking $f_{\text{CE}} = 0.2$, $n_{\text{s,MW}} = 10^{11}$, $\bar{t} = 10^{10}$ years, and $t_{\text{CE}} = 1$ year, yields $N_{\text{MW}} \sim 2$ CEs occurring in the Milky Way. Extending this number to the Local Group can be approximated by $N_{\text{LG}} \sim (\Upsilon_{\text{LG}}/\Upsilon_{\text{MW}}) N_{\text{MW}}$ where Υ_{LG} is the mass-to-light ratio in the Local Group and Υ_{MW} is the mass-to-light ratio in the Milky Way. Adopting $\Upsilon_{\text{LG}} \sim 2\Upsilon_{\text{MW}}$ yields $N_{\text{LG}} \sim 4$ (Van den Bergh, 1999; Overduin and Wesson, 2004). Given that Rubin could detect CEs to ~ 8 Mpc, we calculate an overall conservative CE number as $N_{8\text{Mpc}} \sim (\Upsilon_{8\text{Mpc}}/\Upsilon_{\text{MW}}) N_{\text{MW}} \sim 130$ (Karachentsev et al., 2004) which would correspond to an approximate rate of one CE every three days.

6. Conclusions

In this work, we present observational signatures of convective common envelopes and demonstrate that such events will be visible by the Rubin Observatory's Simonyi Survey Telescope. Following the dynamics initially described in Wilson and Nordhaus (2019), we determine the region within the primary's envelope where convection transports liberated orbital energy to the surface faster than the orbit decays. In this regime, the CE self-regulates, convectively cools, and qualitatively differs from non-convective CEs as the orbital energy is lost from the system. From this, we construct light curves for convective common envelopes, and compare these results to the upcoming observatory's specifications. In particular, this work found that:

1. Light curves for CE targets change when convection is considered. Including convection increases the duration

of the observable light curve, with the more massive primaries being more strongly affected by convective effects than the less massive primaries (see Figure 4).

2. The Simonyi Survey Telescope can detect these events, not only in our galaxy but throughout the Local Group as well. This will establish observational constraints that can help distinguish what role convection has in CE evolution (see Figures 5, 6).

These findings motivate using LSST data to identify common envelope transient events and suggest a likelihood of observation. Due to its modular structure, the method described in this work can be applied to current instruments as well, as it is possible CE events could be identifiable within archival data.

The models produced here were pairings of low-mass stars and companions with well-defined parameters that would unbind the primary star’s envelope while allowing the convective motions within the CE to remain subsonic (Figure 2). Future work specific to the observatory includes producing models for other pairings that would be visible given the telescope’s parameters, such that a wider range of CE events can be identified once Rubin comes online. Because this same process can be applied to currently available data, confirmation of convective CE events can be done with any instrument sensitive to these parameters.

Further work also includes understanding the effects of convection on light curves of massive stars. This would improve our understanding of CE evolution overall, as stars with masses greater than those described in this work have convective regions that do not penetrate as deeply into the primary’s envelope (Wilson and Nordhaus, 2022). The discrepancy in how efficiently orbital energy can be tapped to drive ejection between low-mass and high-mass CEs has already had success explaining post-CE population distributions. Identifying objects undergoing such physical processes in real time would provide useful observational constraints on CE physics.

CE evolution is anticipated to occur on timescales well within the scope of the Rubin observatory, which will observe the southern sky every few days over a decade in the visible light spectrum (Željko Ivezić et al., 2019). While many post-CE objects have been, or are being, identified (Grondin et al., 2024), targets currently undergoing CE evolution have yet to be recognized due to the short duration of the CE phase and the obscuring envelope of the primary. The findings outlined in this work help overcome these difficulties, and can aid in identification, regardless of the instrument.

Acknowledgements

The authors acknowledge Maria Drout, Phil Muirhead, Stefani Grondin, Josh Faber, Joel Kastner, Jared Goldberg, Matteo Cantiello, and Carlos Badenas for helpful conversation and comments regarding this work. NN is supported by the New York Space Grant Consortium. JN acknowledges support from NSF AST-2009713 and AST-2319326.

7. Data Availability

No new observational data were generated from this research. Data underlying this article is available in the articles and supplementary materials of the referenced papers. Stellar interior models were derived from MESA, which is available at <http://mesa.sourceforge.net>. Filter values for anticipated magnitudes were calculated using resources found on the LSST website, as well as specifications described in Kahn et al. 2010. Additional information is available by request.

References

- Bermúdez-Bustamante, L.C., De Marco, O., Siess, L., Price, D.J., González-Bolívar, M., Lau, M.Y.M., Mu, C., Hirai, R., Danilovich, T., Kasliwal, M.M., 2024. Dust formation in common envelope binary interactions – ii: 3d simulations with self-consistent dust formation. *arXiv* 000, arXiv:2401.03644. URL: <https://ui.adsabs.harvard.edu/abs/2024arXiv240103644B>, doi:10.48550/ARXIV.2401.03644.
- Blagorodnova, N., et al., 2016. Common envelope ejection for a luminous red nova in m101. *ApJ* 834, 107. URL: <http://arxiv.org/abs/1607.08248>, doi:10.3847/1538-4357/834/2/107.
- Bloecker, T., 1995. Stellar evolution of low and intermediate-mass stars. i. mass loss on the agb and its consequences for stellar evolution. - *nasa/ads. Astronomy and Astrophysics* 297, 727.
- Bujarrabal, V., Castro-Carrizo, A., Alcolea, J., Contreras, C.S., 2001. Mass, linear momentum and kinetic energy of bipolar flows in protoplanetary nebulae. *A&A* 377, 868–897. URL: <https://ui.adsabs.harvard.edu/abs/2001A&A...377..868B>, doi:10.1051/0004-6361:20011090.
- Burrows, A., Hubbard, W.B., Saumon, D., Lunine, J.I., 1993. An expanded set of brown dwarf and very low mass star models. *ApJ* 406, 158. URL: <https://ui.adsabs.harvard.edu/abs/1993ApJ...406..158B>, doi:10.1086/172427.
- Canals, P., Torres, S., Soker, N., 2018. Oxygen-neon-rich merger during common envelope evolution. *Monthly Notices of the Royal Astronomical Society* 480, 4519–4525. URL: <https://ui.adsabs.harvard.edu/abs/2018MNRAS.480.4519C>, doi:10.1093/MNRAS/STY2121.
- Chamandy, L., Carroll-Nellenback, J., Blackman, E.G., Frank, A., Tu, Y., Liu, B., Zou, Y., Nordhaus, J., 2023. How negative feedback and the ambient environment limit the influence of recombination in common envelope evolution. *arXiv* URL: <https://arxiv.org/abs/2304.14840v2>.
- Chamandy, L., Frank, A., Blackman, E.G., Carroll-Nellenback, J., Liu, B., Tu, Y., Nordhaus, J., Chen, Z., Peng, B., 2018a. Accretion in common envelope evolution. *Monthly Notices of the Royal Astronomical Society* 480, 1898–1911. URL: <https://ui.adsabs.harvard.edu/abs/2018MNRAS.480.1898C>, doi:10.1093/MNRAS/STY1950.
- Chamandy, L., Tu, Y., Blackman, E.G., Carroll-Nellenback, J., Frank, A., Liu, B., Nordhaus, J., 2018b. Energy budget and core-envelope motion in common envelope evolution. *Monthly Notices of the Royal Astronomical Society* 486, 1070–1085. URL: <http://arxiv.org/abs/1812.11196>, doi:10.1093/mnras/stz887.
- Chen, Z., Frank, A., Blackman, E.G., Nordhaus, J., Carroll-Nellenback, J., 2017. Mass transfer and disc formation in agb binary systems. *Monthly Notices of the Royal Astronomical Society* 468, 4465–4477. URL: <https://ui.adsabs.harvard.edu/abs/2017MNRAS.468.4465C>, doi:10.1093/mnras/stx680.
- Chen, Z., Ivanova, N., 2024. Bridging the gap between luminous red novae and common envelope evolution: the role of recombination energy and radiation force. *arXiv*.
- Chugai, N.N., 1991. Duration of the plateau stage in type-ii supernovae - *nasa/ads. Soviet Astronomy Letters* 17. URL: <https://ui.adsabs.harvard.edu/abs/1991SvAL...17..210C>.
- Cummings, J.D., Kalirai, J.S., Tremblay, P.E., Ramirez-Ruiz, E., Choi, J., 2018. The white dwarf initial-final mass relation for progenitor stars from 0.85 to 7.5 solar masses. *The Astrophysical Journal* 866, 21. URL: <https://ui.adsabs.harvard.edu/abs/2018ApJ...866...21C>, doi:10.3847/1538-4357/aadfd6.

- Davis, P.J., Kolb, U., Willems, B., 2009. A comprehensive population synthesis study of post-common envelope binaries. *MNRAS* 403, 179–195. URL: <http://arxiv.org/abs/0903.4152>, doi:10.1111/j.1365-2966.2009.16138.x.
- De Marco, O., Passy, J.C., Moe, M., Herwig, F., Low, M.M.M., Paxton, B., 2011. On the alpha formalism for the common envelope interaction. *Monthly Notices of the Royal Astronomical Society* 411, 2277–2292. URL: <https://ui.adsabs.harvard.edu/abs/2011MNRAS.411.2277D>, doi:10.1111/j.1365-2966.2010.17891.x.
- Fabrycky, D., Tremaine, S., 2007. Shrinking binary and planetary orbits by kozai cycles with tidal friction. *The Astrophysical Journal* 669, 1298–1315. URL: <https://ui.adsabs.harvard.edu/abs/2007ApJ...669.1298F>, doi:10.1086/521702.
- Glanz, H., Perets, H.B., 2018. Efficient common-envelope ejection through dust-driven winds. *Monthly Notices of the Royal Astronomical Society: Letters* 478, L12–L17. URL: <https://academic.oup.com/mnras/advance-article/doi/10.1093/mnrasl/ltz065>.
- González-Bolívar, M., De Marco, O., Lau, M.Y.M., Hirai, R., Price, D.J., 2022. Common envelope binary interaction simulations between a thermally pulsating agb star and a low mass companion. *MNRAS* 517, 3181–3199. URL: <https://doi.org/10.1093/mnras/stac2301>, doi:10.1093/mnras/stac2301.
- Grichener, A., Sabach, E., Soker, N., 2018. The limited role of recombination energy in common envelope removal. *Monthly Notices of the Royal Astronomical Society* 478, 1818–1824. URL: <https://ui.adsabs.harvard.edu/abs/2018MNRAS.478.1818G>, doi:10.1093/mnras/sty1178.
- Grondin, S., Drout, M., Nordhaus, J., Muirhead, P., Speagle, J., Chornock, R., 2024. The first catalogue of candidate white dwarf-main sequence binaries in open star clusters: A new window into common envelope evolution. Submitted to *ApJ*.
- Guidarelli, G., Nordhaus, J., Carroll-Nellenback, J., Chamanady, L., Frank, A., Blackman, E.G., 2022. The formation of discs in the interior of agb stars from the tidal disruption of planets and brown dwarfs. *MNRAS* 511, 5994–6000. URL: <https://doi.org/10.1093/mnras/stac463>, doi:10.1093/mnras/stac463.
- Guidarelli, G., Nordhaus, J., Chamanady, L., Chen, Z., Blackman, E.G., Frank, A., Carroll-Nellenback, J., Liu, B., 2019. Hydrodynamic simulations of disrupted planetary accretion discs inside the core of an agb star. *MNRAS* 490, 1179–1185. URL: <https://academic.oup.com/mnras/article/490/1/1179/5572482>, doi:10.1093/mnras/stz2641.
- Hatfull, R.W., Ivanova, N., Lombardi, J.C., 2021. Simulating a stellar contact binary merger - i. stellar models. *Monthly Notices of the Royal Astronomical Society* 507, 385–397. URL: <https://ui.adsabs.harvard.edu/abs/2021MNRAS.507...385H>, doi:10.1093/mnras/stab2140.
- Hollands, M.A., Littlefair, S.P., Parsons, S.G., 2023. Measuring the initial-final mass-relation using wide double white dwarf binaries from gaia dr3. *MNRAS* 000, 1–26. URL: <https://arxiv.org/abs/2311.14801v1>.
- Iaconi, R., De Marco, O., 2019. Speaking with one voice: Simulations and observations discuss the common envelope alpha parameter. *Monthly Notices of the Royal Astronomical Society* 490, 2550–2566. URL: <https://ui.adsabs.harvard.edu/abs/2019MNRAS.490.2550I>, doi:10.1093/mnras/stz2756.
- Iben, I., Tutukov, A.V., 1984. The evolution of low-mass close binaries influenced by the radiation of gravitational waves and by a magnetic stellar wind. *The Astrophysical Journal* 284, 719–744. URL: <https://ui.adsabs.harvard.edu/abs/1984ApJ...284..719I>, doi:10.1086/162455.
- Icko, J.I., Livio, M., 1993. Common envelopes in binary star evolution. *Publications of the Astronomical Society of the Pacific* 105, 1373. doi:10.1086/133321.
- Ivanova, N., 2018. On the use of hydrogen recombination energy during common envelope events. *The Astrophysical Journal* 858, L24. URL: <https://ui.adsabs.harvard.edu/abs/2018ApJ...858L..24I>, doi:10.3847/2041-8213/aac101.
- Ivanova, N., Justham, S., Chen, X., De Marco, O., Fryer, C.L., Gaburov, E., Ge, H., Glebbeek, E., Han, Z., Li, X.D., Lu, G., Marsh, T., Podsiadlowski, P., Potter, A., Soker, N., Taam, R., Tauris, T.M., van den Heuvel, E.P.J., Webbink, R.F., 2012. Common envelope evolution: Where we stand and how we can move forward. *The Astronomy and Astrophysics Review* 21, 1–83. URL: <http://arxiv.org/abs/1209.4302>, doi:10.1007/s00159-013-0059-2.
- Ivanova, N., Justham, S., Nandez, J.L.A., Lombardi, J.C., 2013. Identification of the long-sought common-envelope events. *Science* 339, 433–435. URL: <https://ui.adsabs.harvard.edu/abs/2013Sci...339.433I>, doi:10.1126/science.1225540.
- Ivanova, N., Justham, S., Podsiadlowski, P., 2015. On the role of recombination in common-envelope ejections. *Monthly Notices of the Royal Astronomical Society* 447, 2181–2197. URL: <https://ui.adsabs.harvard.edu/abs/2015MNRAS.447.2181I>, doi:10.1093/mnras/stu2582.
- Željko Ivezić, et al., 2019. Lsst: From science drivers to reference design and anticipated data products. *The Astrophysical Journal* 873, 111. URL: <https://ui.adsabs.harvard.edu/abs/2019ApJ...873..111I>, doi:10.3847/1538-4357/ab042c.
- Kahn, S.M., Kurita, N., Gilmore, K., Nordby, M., O'Connor, P., Schindler, R., Oliver, J., Berg, R.V., Olivier, S., Riot, V., Antilogus, P., Schalk, T., Huffer, M., Bowden, G., Singal, J., Foss, M., 2010. Design and development of the 3.2 gigapixel camera for the large synoptic survey telescope. *SPIE* 7735, 77350J. URL: <https://ui.adsabs.harvard.edu/abs/2010SPIE.7735E..0JK>, doi:10.1117/12.857920.
- Karachentsev, I.D., Karachentseva, V.E., Huchtmeier, W.K., Makarov, D.I., 2004. A catalog of neighboring galaxies. *The Astronomical Journal*, Volume 127, Issue 4, pp. 2031–2068. 127, 2031. URL: <https://ui.adsabs.harvard.edu/abs/2004AJ...127.2031K>, doi:10.1086/382905.
- Kasen, D., Woosley, S.E., 2009. Type ii supernovae: Model light curves and standard candle relationships. *The Astrophysical Journal* 703, 2205–2216. doi:10.1088/0004-637X/703/2/2205.
- Kashi, A., Soker, N., 2018. Counteracting tidal circularization with the grazing envelope evolution. *Monthly Notices of the Royal Astronomical Society* 480, 3195–3200. URL: <https://academic.oup.com/mnras/article/480/3/3195/5066190>, doi:10.1093/mnras/sty2115.
- Kochanek, C.S., Adams, S.M., Belczynski, K., 2014. Stellar mergers are common. *Monthly Notices of the Royal Astronomical Society* 443, 1319–1328. doi:10.1093/MNRAS/STU1226.
- Kruckow, M.U., Tauris, T.M., Langer, N., Kramer, M., Izzard, R.G., 2018. Progenitors of gravitational wave mergers: Binary evolution with the stellar grid-based code combine. *Monthly Notices of the Royal Astronomical Society* 481, 1908–1949. URL: <https://ui.adsabs.harvard.edu/abs/2018MNRAS.481.1908K>, doi:10.1093/mnras/sty2190.
- Kuruwita, R.L., Staff, J., De Marco, O., 2016. Considerations on the role of fall-back discs in the final stages of the common envelope binary interaction. *Monthly Notices of the Royal Astronomical Society* 461, 486–496. URL: <https://academic.oup.com/mnras/article/461/1/486/2595328>, doi:10.1093/mnras/stw1414.
- Lau, M.Y., Hirai, R., González-Bolívar, M., Price, D.J., De Marco, O., Mandel, I., 2022. Common envelopes in massive stars: towards the role of radiation pressure and recombination energy in ejecting red supergiant envelopes. *Monthly Notices of the Royal Astronomical Society* 512, 5462–5480. URL: <https://academic.oup.com/mnras/article/512/4/5462/6502364>, doi:10.1093/mnras/stac049.
- Livio, M., Soker, N., 1988. The common envelope phase in the evolution of binary stars. *The Astrophysical Journal* 329, 764. URL: <https://ui.adsabs.harvard.edu/abs/1988ApJ...329..764L>, doi:10.1086/166419.
- Lorenzo, M., Teyssier, D., Bujarrabal, V., García-Lario, P., Alcolea, J., Verdugo, E., Marston, A., 2021. Fast outflows in protoplanetary nebulae and young planetary nebulae observed by herschel /hifi. *Astronomy and Astrophysics* 649, A164. URL: <https://ui.adsabs.harvard.edu/abs/2021A&A...649A.164L>, doi:10.1051/0004-6361/202039592.
- Macleod, M., Cantiello, M., Soares-Furtado, M., 2018. Planetary engulfment in the hertzsprung-russell diagram. *The Astrophysical Journal Letters* 853, L1. URL: <https://doi.org/10.3847/2041-8213/aaa5fa>, doi:10.3847/2041-8213/aaa5fa.
- Matsumoto, T., Metzger, B.D., 2022. Light-curve model for luminous red novae and inferences about the ejecta of stellar mergers. *ApJ* 938, 5. doi:10.3847/1538-4357/ac6269.
- Michaely, E., Perets, H.B., 2016. Tidal capture formation of low-mass x-ray binaries from wide binaries in the field. *Monthly Notices of the Royal Astronomical Society* 458, 4188–4197. URL: <https://ui.adsabs.harvard.edu/abs/2016MNRAS.458.4188M>, doi:10.1093/mnras/stw368.
- Nandez, J.L.A., Ivanova, N., Lombardi, J.C., 2015. Recombination energy in double white dwarf formation. *Monthly Notices of the Royal Astronomical Society* 450, L39–L43. URL: <http://arxiv.org/abs/1503.02750>, doi:10.1093/mnras/ltv043.

Nordhaus, J., Blackman, E.G., 2006. Low-mass binary-induced outflows from asymptotic giant branch stars. *Monthly Notices of the Royal Astronomical Society* 370, 2004–2012. URL: <https://ui.adsabs.harvard.edu/abs/2006MNRAS.370.2004N>, doi:10.1111/j.1365-2966.2006.10625.x.

Nordhaus, J., Blackman, E.G., Frank, A., 2007. Isolated vs. common envelope dynamos in planetary nebula progenitors. *Monthly Notices of the Royal Astronomical Society* 376, 599–608. URL: <http://arxiv.org/abs/astro-ph/0609726>, doi:10.1111/j.1365-2966.2007.11417.x.

Nordhaus, J., Spiegel, D.S., 2013. On the orbits of low-mass companions to white dwarfs and the fates of the known exoplanets. *Monthly Notices of the Royal Astronomical Society* 432, 500–505. URL: <https://ui.adsabs.harvard.edu/abs/2013MNRAS.432..500N>, doi:10.1093/mnras/stt569.

Nordhaus, J., Spiegel, D.S., Ibgui, L., Goodman, J., Burrows, A., 2010. Tides and tidal engulfment in post-main sequence binaries: Period gaps for planets and brown dwarfs around white dwarfs. *MNRAS* 408, 631–641. URL: <http://arxiv.org/abs/1002.2216>, doi:10.1111/j.1365-2966.2010.17155.x.

Nordhaus, J., Wellons, S., Spiegel, D.S., Metzger, B.D., Blackman, E.G., 2011. Formation of high-field magnetic white dwarfs from common envelopes. *Proceedings of the National Academy of Sciences of the United States of America* 108, 3135–3140. URL: <https://ui.adsabs.harvard.edu/abs/2011PNAS..108.3135N>, doi:10.1073/pnas.1015005108.

Ohlmann, S.T., Röpke, F.K., Pakmor, R., Springel, V., 2015. Hydrodynamic moving-mesh simulations of the common envelope phase in binary stellar systems. *The Astrophysical Journal Letters* 816, L9. doi:10.3847/2041-8205/816/1/L9.

Overduin, J.M., Wesson, P.S., 2004. Dark matter and background light. *Physics Reports* 402, 267–406. doi:10.1016/J.PHYSREP.2004.07.006.

Paczynski, B., 1976. Structure and evolution of close binary systems, D. Reidel Publishing Co. pp. 75–80. URL: <https://ui.adsabs.harvard.edu/abs/1976IAUS...73...75P>.

Park, K., Bogdanović, T., 2017. Gaseous dynamical friction in presence of black hole radiative feedback. *The Astrophysical Journal* 838, 103. URL: <https://iopscience.iop.org/article/10.3847/1538-4357/aa65ce>, doi:10.3847/1538-4357/AA65CE.

Passy, J.C., De Marco, O., Fryer, C.L., Herwig, F., Diehl, S., Oishi, J.S., Low, M.M.M., Bryan, G.L., Rockefeller, G., 2011. Simulating the common envelope phase of a red giant using sph and uniform grid codes. *The Astrophysical Journal* 744, 52. URL: <http://arxiv.org/abs/1107.5072>, doi:10.1088/0004-637X/744/1/52.

Paxton, B., Bildsten, L., Dotter, A., Herwig, F., Lesaffre, P., Timmes, F., 2011. Modules for experiments in stellar astrophysics (mesa). *Astrophysical Journal, Supplement Series* 192, 3. URL: <https://ui.adsabs.harvard.edu/abs/2011ApJS...192...3P>, doi:10.1088/0067-0049/192/1/3.

Paxton, B., Schwab, J., Bauer, E.B., Bildsten, L., Blinnikov, S., Duffell, P., Farmer, R., Goldberg, J.A., Marchant, P., Sorokina, E., Thoul, A., Townsend, R.H.D., Timmes, F.X., 2018. Modules for experiments in stellar astrophysics (mesa): Convective boundaries, element diffusion, and massive star explosions. *ApJS* 234, 34. URL: <http://arxiv.org/abs/1710.08424>, doi:10.3847/1538-4365/aaa5a8.

Politano, M., Weiler, K.P., 2007. Population synthesis studies of close binary systems using a variable common envelope efficiency parameter: I. dependence upon secondary mass. *The Astrophysical Journal* 665, 663–679. URL: <http://arxiv.org/abs/astro-ph/0702662>, doi:10.1086/518997.

Popov, D.V., 1993. An analytical model for the plateau stage of type ii supernovae. *The Astrophysical Journal* 414, 712. doi:10.1086/173117.

Reichardt, T.A., De Marco, O., Iaconi, R., Chamandy, L., Price, D.J., 2020. The impact of recombination energy on simulations of the common-envelope binary interaction. *Monthly Notices of the Royal Astronomical Society* 494, 5333–5349. URL: <https://academic.oup.com/mnras/article/494/4/5333/5819450>, doi:10.1093/MNRAS/STAA937.

Reimers, D., 1975. Circumstellar absorption lines and mass loss from red giants. - nasa/ads. *Memoires of the Societe Royale des Sciences de Liege* 8, 369–382. URL: <https://ui.adsabs.harvard.edu/abs/1975MSRSL...8...369R>.

Reyes-Ruiz, M., López, J.A., 1999. Accretion disks in pre-planetary nebulae. *The Astrophysical Journal, Volume 524, Issue 2*, pp. 952–960. 524, 952. URL: <https://ui.adsabs.harvard.edu/abs/1999ApJ...524..952R>, doi:10.1086/307827.

Ricker, P.M., Taam, R.E., 2008. The interaction of stellar objects within a common envelope. *The Astrophysical Journal* 672, L41–L44. URL: <https://iopscience.iop.org/article/10.1086/526343>, doi:10.1086/526343.

Ricker, P.M., Taam, R.E., 2012. An amr study of the common-envelope phase of binary evolution. *The Astrophysical Journal* 746, 74. URL: <https://ui.adsabs.harvard.edu/abs/2012ApJ...746...74R>, doi:10.1088/0004-637X/746/1/74.

Röpke, F.K., De Marco, O., 2023. Simulations of common-envelope evolution in binary stellar systems: physical models and numerical techniques. *Living Reviews in Computational Astrophysics* 9, 1–129. URL: <https://doi.org/10.1007/s41115-023-00017-x>, doi:10.1007/s41115-023-00017-x.

Sabach, E., Hillel, S., Schreier, R., Soker, N., 2017. Energy transport by convection in the common envelope evolution. *Monthly Notices of the Royal Astronomical Society* 472, 4361–4367. URL: <https://ui.adsabs.harvard.edu/abs/2017MNRAS.472.4361S>, doi:10.1093/MNRAS/STX2272.

Schreier, R., Hillel, S., Shiber, S., Soker, N., 2021. Simulating highly eccentric common envelope jet supernova impostors. *Monthly Notices of the Royal Astronomical Society* 508, 2386–2398. URL: <https://academic.oup.com/mnras/article/508/2/2386/6373468>, doi:10.1093/MNRAS/STAB2687.

Shappee, B.J., Thompson, T.A., 2013. The mass-loss-induced eccentric kozai mechanism: A new channel for the production of close compact object-stellar binaries. *The Astrophysical Journal* 766, 64. URL: <https://ui.adsabs.harvard.edu/abs/2013ApJ...766...64S>, doi:10.1088/0004-637X/766/1/64.

Shima, E., Matsuda, T., Takeda, H., Sawada, K., 1985. Hydrodynamic calculations of axisymmetric accretion. *5MNRAS.217..367S Mon. Not. R. astr. Soc* 217, 367–386.

Soker, N., 2015. Close stellar binary systems by grazing envelope evolution. *The Astrophysical Journal* 800, 114. doi:10.1088/0004-637X/800/2/114.

Soker, N., Grichener, A., Sabach, E., 2018. Radiating the hydrogen recombination energy during common envelope evolution. *The Astrophysical Journal* 863, L14. URL: <https://ui.adsabs.harvard.edu/abs/2018ApJ...863L..14S>, doi:10.3847/2041-8213/aad736.

Thompson, T.A., 2011. Accelerating compact object mergers in triple systems with the kozai resonance: A mechanism for “prompt” type ia supernovae, gamma-ray bursts, and other exotica. *The Astrophysical Journal* 741, 82. URL: <https://ui.adsabs.harvard.edu/abs/2011ApJ...741...82T>, doi:10.1088/0004-637X/741/2/82.

Toonen, S., Hollands, M., Gänsicke, B.T., Boekholt, T., 2017. The binarity of the local white dwarf population. *Astronomy and Astrophysics* 602. doi:10.1051/0004-6361/201629978.

Toonen, S., Nelemans, G., 2013. The effect of common-envelope evolution on the visible population of post-common-envelope binaries. *Astronomy & Astrophysics* 557, A87. URL: <http://arxiv.org/abs/1309.0327>, doi:10.1051/0004-6361/201321753.

Tutukov, A., Yungelson, L., 1979. Evolution of massive common envelope binaries and mass loss. - nasa/ads, D. Reidel Publishing Co. URL: <https://ui.adsabs.harvard.edu/abs/1979IAUS...83..401T>.

Valsan, V., Borges, S.V., Prust, L., Chang, P., 2023. Envelope ejection and the transition to homologous expansion in common-envelope ev ents. *MNRAS* 526, 5365–5373. URL: <https://doi.org/10.1093/mnras/stad3075>, doi:10.1093/mnras/stad3075.

Van den Bergh, S., 1999. The local group of galaxies. *Astronomy and Astrophysics Review* 9, 273–318. URL: <https://link.springer.com/article/10.1007/s001590050019>, doi:10.1007/S001590050019/METRICS.

van Winckel, H., 2003. Post-agb stars. *ARA&A* 41, 391–427. URL: <https://ui.adsabs.harvard.edu/abs/2003ARA&A...41..391V>, doi:10.1146/ANNUREV.ASTRO.41.071601.170018.

Villaver, E., Livio, M., 2009. The orbital evolution of gas giant planets around giant stars. *The Astrophysical Journal* 705, L81–L85. URL: <https://ui.adsabs.harvard.edu/abs/2009ApJ...705L..81V>, doi:10.1088/0004-637X/705/1/L81.

Webbink, R.F., 1984. Double white dwarfs as progenitors of r coronae borealis stars and type i supernovae. *The Astrophysical Journal* 277, 355–360. URL: <https://ui.adsabs.harvard.edu/abs/1984ApJ...277..355W>.

- .355W, doi:10.1086/161701.
- Wilson, E.C., Nordhaus, J., 2019. The role of convection in determining the ejection efficiency of common envelope interactions. *Monthly Notices of the Royal Astronomical Society* 485, 4492–4501. doi:10.1093/MNRAS/STZ601.
- Wilson, E.C., Nordhaus, J., 2020. Convection and spin-up during common envelope evolution: The formation of short-period double white dwarfs. *Monthly Notices of the Royal Astronomical Society* 497, 1895–1903. URL: <https://ui.adsabs.harvard.edu/abs/2020MNRAS.497.1895W>, doi:10.1093/mnras/staa2088.
- Wilson, E.C., Nordhaus, J., 2022. Convection reconciles the difference in efficiencies between low-mass and high-mass common envelopes. *Monthly Notices of the Royal Astronomical Society* URL: <http://arxiv.org/abs/2203.06091>.
- Zapolsky, H.S., Salpeter, E.E., 1969. The mass-radius relation for cold spheres of low mass. *ApJ* 158, 809. URL: <https://ui.adsabs.harvard.edu/abs/1969ApJ...158..809Z>, doi:10.1086/150240.
- Zorotovic, M., Schreiber, M.R., Gänsicke, B.T., Gómez-Morán, A.N., 2010. Post-common-envelope binaries from sdss. ix: Constraining the common-envelope efficiency. *Astronomy and Astrophysics* 520, A86. URL: <http://arxiv.org/abs/1006.1621>, doi:10.1051/0004-6361/200913658.